Boson peak in the vibrational spectra of glasses

Avraham Moriel [1,*] Edan Lerner,[2] and Eran Bouchbinder [1,†]
[1]*Chemical and Biological Physics Department, Weizmann Institute of Science, Rehovot 7610001, Israel*
[2]*Institute for Theoretical Physics, University of Amsterdam, Science Park 904, Amsterdam, Netherlands*

(Received 18 October 2023; accepted 22 March 2024; published 15 April 2024)

A hallmark of glasses is an excess of low-frequency, nonphononic vibrations. It is manifested as a terahertz peak—the boson peak—in the ratio of the vibrational density of state (VDoS) and Debye's VDoS of phonons. Here, using experimental data, extensive computer simulations, and a mean-field model, we show that the nonphononic part of the VDoS itself features both a universal power-law tail and a peak at higher frequencies, entirely accounted for by quasilocalized nonphononic vibrations, whose existence and spectra power-law tail were recently established in computer glasses. We rationalize the variation of the peak's frequency and magnitude with glasses' thermal history, which is much weaker than the variation of the tail and may follow an opposite trend, and show that the peak's modes are composed of many spatially coupled quasilocalized nonphononic vibrations. Our results shed light on the origin, nature, and properties of the boson peak in glasses.

DOI: 10.1103/PhysRevResearch.6.023053

I. INTRODUCTION

The glassy state of matter, generically formed by quickly cooling a liquid to avoid crystallization, still poses fundamental scientific challenges [1–5]. The fast cooling leads to a self-organized disordered solid—a glass—that lacks the long-range order of crystalline solids [6]. The disordered and nonequilibrium nature of glasses endows them with unique physical properties, different from their crystalline counterparts. Of particular importance are the low-frequency vibrational spectra, which control various mechanical, transport, and thermodynamic properties of solids [7–13].

The low-frequency vibrational spectra of solids—either crystalline or glassy—contain phonons, which are extended vibrations emerging from global symmetries, independently of the underlying material structure [14]. Low-frequency phonons are well described by Debye's vibrational density of state (VDoS), $\mathcal{D}_{\rm D}(\omega) = A_{\rm D}\,\omega^2$ (in three dimensions), where ω is the vibrational (angular) frequency and $A_{\rm D}$ is a prefactor that depends on the elastic properties of the solid.

The low-frequency vibrational spectra of glasses, however, are known to universally feature also other, nonphononic, modes. This is commonly—yet not exclusively (see [15,16])—established by dividing the VDoS (measured by various scattering techniques [17,18]), $\mathcal{D}(\omega)$, by Debye's phononic VDoS, $\mathcal{D}_{\rm D}(\omega) \sim \omega^2$. The reduced VDoS $\mathcal{D}(\omega)/\omega^2$ universally deviates from a constant at low frequencies and features a peak in the terahertz regime, known as the boson peak—a hallmark of glasses [19–31]. Yet, despite extensive efforts, the origin, nature, and properties of the nonphononic boson peak vibrations remain highly debated [32–39].

Significant recent progress [40–45] elucidated the nature and properties of the low-frequency tail, $\omega \to 0$, of the nonphononic part of the VDoS $\mathcal{D}_{\rm G}(\omega)$. By disentangling extended phononic and quasilocalized nonphononic vibrations in computer glasses, the latter were shown to follow a universal non-Debye VDoS $\mathcal{D}_{\rm G}(\omega) = A_{\rm g}\,\omega^4$ in the $\omega \to 0$ limit, below the boson peak [40,45]. Here, $A_{\rm g}$ is a nonuniversal prefactor that depends on the glass nonequilibrium history and its emerging disordered state [45,46]. These quasilocalized nonphononic vibrations feature a localized core of linear size of about ten atoms, where displacement amplitudes are large and highly disordered in orientation (i.e., nonaffine), and power-law decaying displacements away from the core [45] [see Fig. 1(a)].

Very recent numerical evidence in two-dimensional computer glasses indicates that quasilocalized nonphononic vibrations also populate the boson peak regime [38], at frequencies significantly larger than those of the $\omega \to 0$ tail. These preliminary observations mark the need to understand the properties of the nonphononic VDoS $\mathcal{D}_{\rm G}(\omega)$ in a unified manner based on quasilocalized nonphononic vibrations, over a larger range of vibrational frequencies ω, extending to the boson peak regime.

Here, using experimental data, extensive atomistic computer simulations, and solutions of a mean-field model of interacting glassy vibrations, we show that the nonphononic part of the VDoS $\mathcal{D}_{\rm G}(\omega)$ features both a universal $\sim\omega^4$ tail and an intrinsic peak, entirely accounted for by quasilocalized nonphononic vibrations. The peak's frequency and magnitude mildly increase with decreasing state of glassy disorder (e.g., controlled by thermal annealing and quantified as explained in detail in Appendix B 2), while the $\sim\omega^4$ tail is strongly suppressed, in qualitative agreement with the predictions of the

*Current address: Department of Mechanical and Aerospace Engineering, Princeton University, Princeton, New Jersey 08544, USA.
†eran.bouchbinder@weizmann.ac.il

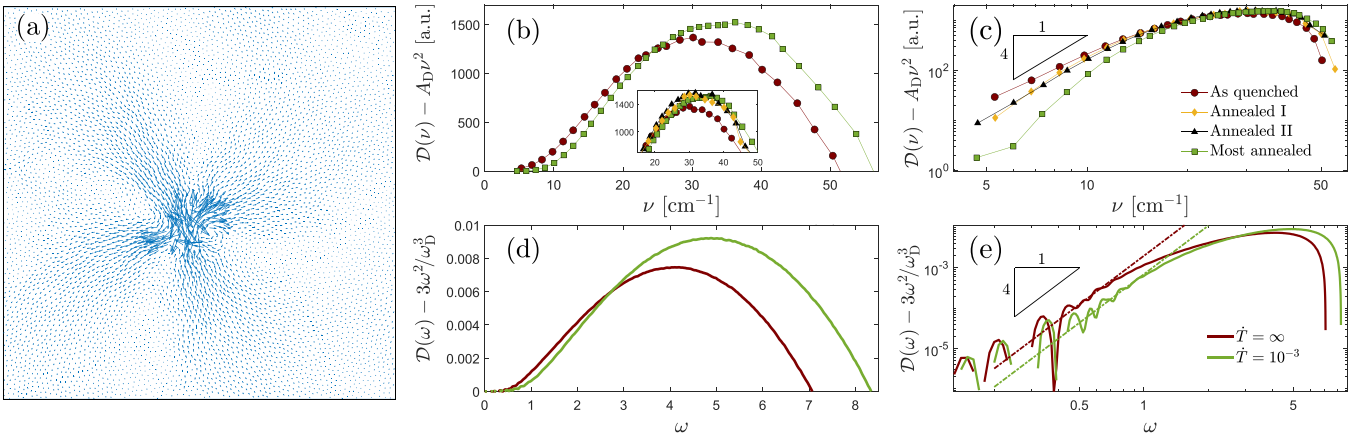

FIG. 1. (a) A quasilocalized vibration extracted from the universal $\sim\omega^4$ tail of the nonphononic VDoS of a two-dimensional computer glass [45]. The arrows represent the atomic displacements within the vibrational mode, which features a localized core of linear size of about ten atoms, where displacement amplitudes are large and highly disordered in orientation. Away from the core, displacements decay as a power law and feature a quadrupolar azimuthal dependence. A two-dimensional example is used for visual clarity. (b) The nonphononic VDoS $\mathcal{D}_G(\nu) \equiv \mathcal{D}(\nu) - A_D\,\nu^2$ of B_2O_3 glass samples, reported in [25] for different thermal annealing conditions and water content. Shown are the data for the as quenched and most annealed samples [see legend on panel (c)]. In [25], $\mathcal{D}(\nu)/\nu^2$ [note $\mathcal{D}(\nu)$ is denoted as $g(\nu)$ therein] and A_D are separately reported, but not $\mathcal{D}_G(\nu)$ itself. $\mathcal{D}_G(\nu)$ reveals a peak, which increases in magnitude and shifts to higher frequencies with increased thermal annealing (corresponding to less disordered glassy states). Data for intermediate annealed samples are added in the inset [see legend in panel (c)]. (c) The same as the inset of panel (b), but on a double-logarithmic scale. The small ν tail approximately reveals the universal $\sim\nu^4$ behavior (see power-law triangle), in the most pronounced manner for the two intermediate annealed samples. Moreover, the amplitude of the tail is strongly suppressed upon annealing, in sharp contrast to the mild increase ν_p and $\mathcal{D}_G(\nu_p)$ observed in panel (b). (d) $\mathcal{D}_G(\omega) = \mathcal{D}(\omega) - 3\omega^2/\omega_D^3$ using a canonical computer glass made of 4×10^6 atoms (see Appendix A 2), where ω_D is Debye's frequency and $A_D = 3/\omega_D^3$. The two curves correspond to different thermal histories—one to an instantaneous quench through the glass transition, $\dot{T} = \infty$, and the other to a smaller quench rate, $\dot{T} = 10^{-3}$ [see legend in panel (e)]. All quantities are reported in simulational units (Appendix A 2). (e) The same as panel (d), but on a double-logarithmic scale. The dashed lines of slope 4 (see power-law triangle) are guides to the eye that indicate the universal $\sim\omega^4$ tail. At the lower end of the VDoS, relics of discrete phonon bands are observed, which are a finite-size effect [47]. Comparing the simulational results in panels (d) and (e) to the experimental results in panels (b) and (c) reveals clear similarities, despite the inherent size limitation in the former.

mean-field model of interacting quasilocalized vibrations. The model thus provides a unified picture of the low-frequency properties of the nonphononic VDoS $\mathcal{D}_G(\omega)$, both the universal $\sim\omega^4$ tail and the peak regimes. Finally, the number of spatially coupled quasilocalized nonphononic vibrations that compose the peak's modes is predicted as a function of ω, and found to be in qualitative agreement with very recent observations. Overall, our results shed important light on the origin, nature, and salient properties of the boson peak in glassy solids.

II. FORM OF THE NONPHONONIC PART OF THE VDOS

The common practice for characterizing the boson peak is through the reduced VDoS $\mathcal{D}(\omega)/\omega^2$, where $\mathcal{D}_D(\omega) \sim \omega^2$ stands for Debye's VDoS of phonons. However, in view of the major recent progress in understanding the universal $\sim\omega^4$ tail of the nonphononic VDoS $\mathcal{D}_G(\omega)$, populated by quasilocalized vibrations [see Fig. 1(a)], we follow [15,16] and shift the focus to $\mathcal{D}_G(\omega)$, aiming to understand its generic properties also above the $\sim\omega^4$ tail. $\mathcal{D}_G(\omega)$ is proposed to be extracted according to $\mathcal{D}_G(\omega) = \mathcal{D}(\omega) - A_D\,\omega^2$, suggesting that as far as the number of vibrational modes per frequency ω is concerned, quasilocalized nonphononic vibrations and phonons make additive contributions to $\mathcal{D}(\omega)$ (while it is well established that phononic and nonphononic modes do hybridize/mix in space [38,47]).

The importance of considering $\mathcal{D}_G(\omega)$ (termed e-VDoS in [15]) instead of $\mathcal{D}(\omega)/\omega^2$ has been highlighted in [15], along with the associated experimental difficulties. In particular, the challenge is to obtain experimental measurements in glassy samples where disorder is systematically controlled, and where the prefactor A_D in Debye's VDoS of phonons $\mathcal{D}_D(\omega) = A_D\,\omega^2$ is extracted. Moreover, if the $\sim\omega^4$ tail of $\mathcal{D}_G(\omega)$ is to be revealed, then $\mathcal{D}(\omega)$ should be measured down to sufficiently small ω. Meeting these challenges is rare. Consequently, our next goal was to perform an extensive literature search for such experimental data, aiming to reanalyze them in view of the above ideas.

The experiments of [24,25] report on the VDoS of boron-oxide (B_2O_3) glass samples for different thermal histories and water content, as well as on Debye's prefactor A_D, and hence are particularly important here. The vibrational spectra therein are reported in terms of the (Raman) wave-number shift ν (in units of cm^{-1}), rather than in terms of ω, i.e., $\mathcal{D}(\nu)$ [in [25] the notation $g(\nu)$, not used here, is employed]. Note that ω and ν are linearly related, and in particular that $\omega = 1$ THz corresponds to $\nu = 33.3$ cm^{-1}. Different thermal histories are realized by subjecting as quenched B_2O_3 glass samples to various annealing treatments, i.e., annealing at different temperatures in the vicinity of the glass temperature T_g for different times. The annealed samples give rise to less disordered, denser glassy states compared to the as quenched sample. Moreover, water content ("wet samples") gives rise

to even denser and more rigid glassy states, effectively corresponding to deeper annealing.

Importantly, in addition to measuring $\mathcal{D}(\nu)$ for each glass sample, Debye's prefactor $A_{\rm D}$ was also extracted (Appendix A 1). In Fig. 1(b), we present $\mathcal{D}_{\rm G}(\nu) \equiv \mathcal{D}(\nu) - A_{\rm D}\,\nu^2$ for the as quenched and most annealed samples [see legend in Fig. 1(c) and Appendix A 1]. First, we observe that $\mathcal{D}_{\rm G}(\nu)$ features a rather symmetric peak in agreement with [15]. Second, the peak's frequency $\nu_{\rm p}$ and magnitude $\mathcal{D}_{\rm G}(\nu_{\rm p})$ mildly increase with annealing (by 20% and 11% relative to the as quenched sample, respectively; see Appendix A 1). The inset also presents data for two intermediate annealed samples [see legend in Fig. 1(c)].

In Fig. 1(c), we present the experimental data shown in the inset of Fig. 1(b) on a double-logarithmic scale. Interestingly, the small ν tail approximately reveals the universal $\sim\nu^4$ behavior, in the most pronounced manner for the two intermediate curves. We present direct experimental evidence for the universal $\sim\omega^4$ tail of the nonphononic VDoS of glasses [48], previously established in computer glasses. Moreover, the tail is strongly suppressed upon annealing. In particular, $\mathcal{D}_{\rm G}(\nu)$ of the most annealed sample is an order of magnitude smaller than that of the as quenched sample at the lowest ν available, in sharp contrast to the mild increase in $\nu_{\rm p}$ and $\mathcal{D}_{\rm G}(\nu_{\rm p})$.

We next set out to test whether these experimental observations are reproduced in atomistic computer glasses. This is a challenge since computer glasses are significantly smaller than laboratory glasses and consequently reveal some finite-size effects, especially in the low-frequency end of vibrational spectra. To try to address this challenge, we considered a canonical computer glass-forming model in three dimensions (see Appendix A 2 for details), composed of 4×10^6 particles. We chose three-dimensional computer glasses due to their relevance to glasses used in laboratory experiments [in contrast to the example presented in Fig. 1(a), and later on in Fig. 4(a), where two-dimensional computer glasses are used for visual clarity].

The size of the computer glasses is chosen to be large enough to restrict the emergence of discrete phonon bands in the VDoS $\mathcal{D}(\omega)$—which are a finite-size effect [47] [the relics of which are seen in Fig. 1(e)] entirely absent from experimental spectra—yet small enough to be computationally feasible and to induce some variability in their degree of structural disorder (Appendixes A 2 and B 1). The latter is achieved by considering an instantaneous quench, leading to more disordered glassy states, and a finite quench, leading to more ordered glassy states (see figure legend). In Figs. 1(d) and 1(e), we present $\mathcal{D}(\omega) - 3\omega^2/\omega_{\rm D}^3$ (where $A_{\rm D} = 3/\omega_{\rm D}^3$, with $\omega_{\rm D}$ being Debye's frequency) in double-linear [Fig. 1(d)] and double-logarithmic [Fig. 1(e)] scales. The salient features of the experimental observations in Figs. 1(b) and 1(c) are reproduced by the computer simulations, despite the inherent size limitation (e.g., setting a bound on the lowest cooling rate); see Appendix B 1.

Our next goal is to gain some theoretical understanding of the main experimental (and simulational) observations. These include the existence of a peak in $\mathcal{D}_{\rm G}(\omega)$ above the $\sim\omega^4$ tail, the mild increase in the peak's frequency $\omega_{\rm p}$ and its magnitude $\mathcal{D}_{\rm G}(\omega_{\rm p})$ with thermal annealing, along with the corresponding strong suppression of the $\sim\omega^4$ tail. Achieving this goal is a major challenge as we currently lack a fundamental theory of glasses in general, and of their low-frequency vibrational spectra in particular. Yet, some very recent developments in formulating and studying mean-field models of quasilocalized nonphononic vibrations may be useful in this context, as we discuss next.

III. MEAN-FIELD MODEL OF QUASILOCALIZED NONPHONONIC VIBRATIONS

We build on a recently formulated mean-field model of quasilocalized nonphononic vibrations [49,50], termed the KHGPS model therein, that reproduced the $\mathcal{D}_{\rm G}(\omega) = A_{\rm g}\omega^4$ VDoS in the $\omega \to 0$ tail below the boson peak, as well as the dependence of the prefactor $A_{\rm g}$ on the disorder parameters of the model. The model envisions small groups of atoms/molecules in an instantaneous snapshot of the liquid state, prior to cooling/quenching through the glass temperature, which feature a collective vibration characterized by a stiffness (spring constant) κ_i, where i is an index of the group (for $\kappa_i > 0$, the vibrational frequency is $\omega_i = \sqrt{\kappa_i}$). Since an instantaneous liquid state features both negative (unstable) and positive local stiffnesses, the probability to find a vanishing κ_i is finite. Consequently, at small positive stiffnesses (frequencies), e.g., within $[0,\ \kappa_0]$, the probability to observe a stiffness κ is given by $p(\kappa) = 1/\kappa_0$, to leading order. The latter implies a liquidlike VDoS $g_0(\omega) = 2\omega/\kappa_0 \equiv 2\omega/\omega_0^2$.

Describing every liquidlike vibration by a single collective coordinate x_i, and considering the lowest stabilizing anharmonicity [49,50], each vibration i is effectively an anharmonic oscillator with energy $\kappa_i x_i^2/2 + x_i^4/24$. Here, $\kappa_i = \omega_i^2$ follows the liquidlike VDoS $g_0(\omega) = 2\omega/\omega_0^2$ and the amplitude of anharmonicity is the same for all oscillators. The oscillators interact among themselves and with the surrounding material, especially as the liquid is quickly cooled/quenched through the glass transition and long-range elasticity builds up. The interactions are random, reflecting the structural disorder in the emerging glass. Moreover, the quench self-organization also gives rise to internal stresses, reflecting glassy frustration, which would tend to displace the oscillators from their reference position.

At the mean-field level, i.e., assuming each oscillator interacts with all of the others, the above physical picture corresponds to the Hamiltonian [33,49–51]

$$H = \frac{1}{2}\sum_i \kappa_i x_i^2 + \frac{1}{24}\sum_i x_i^4 + \sum_{i<j} J_{ij} x_i x_j - h\sum_i x_i\,, \quad (1)$$

of N interacting anharmonic oscillators, with $i = 1 - N$. Here, J_{ij} are Gaussian independent and identically distributed random variables of variance J^2/N for $i \neq j$, representing random bilinear interactions between the oscillators due to structural disorder. h represents internal stresses, which also emerge due to structural disorder, though h itself is taken to be the same for all oscillators. κ_i, as explained above, is drawn from a rather "featureless" liquidlike probability distribution. The minimization of the Hamiltonian in Eq. (1) mimics the quench self-organization process, upon which the oscillators experience displacements and new frequencies ω at

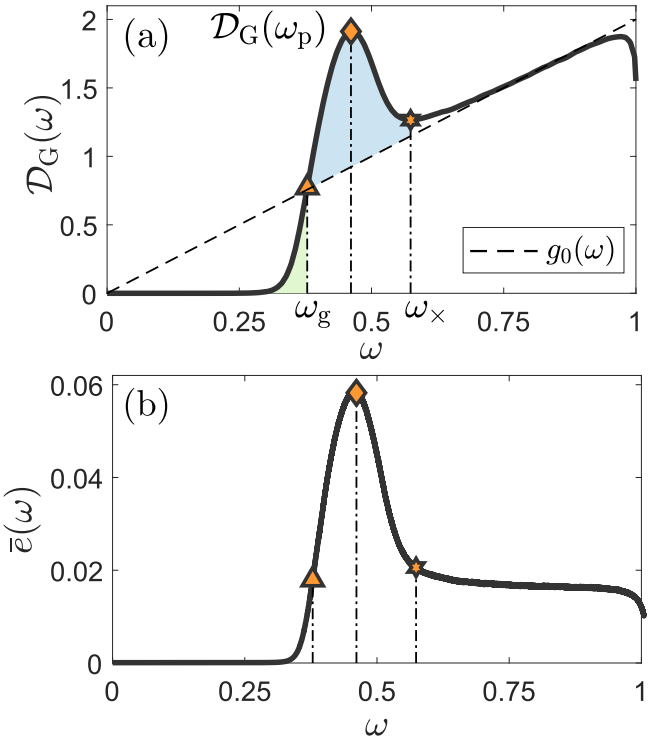

FIG. 2. (a) A representative nonphononic VDoS $\mathcal{D}_G(\omega)$ of the mean-field model of Eq. (1), in the small $y = J/(h^{1/3}\kappa_0^{1/2})$ regime (thick solid line); see Appendix A 3 for details. Here and elsewhere in this paper, we set $\kappa_0 = 1$ (which implies that the largest frequency is $\omega_0 = \sqrt{\kappa_0} = 1$, as shown). $\mathcal{D}_G(\omega)$ attains a local maximum at ω_p, as marked (orange diamond). The thin dashed line corresponds to the initial liquidlike VDoS $g_0(\omega) = 2\omega/\omega_0^2$ (see legend). $\omega_\times$ [orange star, corresponding to the local minimum of $\mathcal{D}_G(\omega)$] marks the frequency above which $g_0(\omega)$ and $\mathcal{D}_G(\omega)$ approximately coincide. ω_g (orange triangle) is a lower intersection frequency of the two curves. The two (blue and green) light shaded regions are discussed in the text. (b) The corresponding averaged participation ratio $\bar{e}(\omega)$; see text for discussion.

the attained minima. The statistics of the latter represent the physical nonphononic VDoS $\mathcal{D}_G(\omega)$.

By studying the statistics of energy minima of Eq. (1) for many independent realizations of the disorder, κ_i and J_{ij}, one obtains the resulting VDoS $\mathcal{D}_G(\omega)$, which represents the VDoS of low-frequency quasilocalized vibrations in glasses in the framework of the model. As such, the minimization of Eq. (1) is viewed as a procedure that transforms a featureless liquidlike VDoS $g_0(\omega)$ into a glassy VDoS $\mathcal{D}_G(\omega)$. In Fig. 2(a), we plot the initial liquidlike VDoS $g_0(\omega)$ (thin dashed line) along with a representative example of the resulting VDoS $\mathcal{D}_G(\omega)$ (thick solid line). The latter features a peak at ω_p of magnitude $\mathcal{D}_G(\omega_p)$, in qualitative agreement with the experimental and simulational observations presented in Fig. 1. Next, we aim at deriving scaling relations for ω_p and $\mathcal{D}_G(\omega_p)$, along with the corresponding properties of the prefactor A_g of the universal $\sim\omega^4$ tail, also observed in Fig. 1.

It has been recently shown in [49] that $A_g \sim \exp(-c_g\kappa_0\, h^{2/3}/J^2)$ (with $c_g \simeq 0.2$), for $y \equiv J/(h^{1/3}\kappa_0^{1/2}) \ll 1$. This exponential variation of A_g with $-y^{-2}$ is reminiscent of the exponential variation of A_g with $-1/T_p$ [46], where T_p is the temperature at which a supercooled liquid falls out of equilibrium during a quench, i.e., it determines the degree of supercooling. The correspondence between the two exponential variations of A_g supports the physical relevance of the model and indicates that a decreasing y implies less disordered glassy states. Moreover, the strong depletion of nonphononic vibrations in the $\mathcal{D}_G(\omega) \sim \omega^4$ tail with decreasing y is similar to the strong reduction in the tail of $\mathcal{D}_G(\omega)$ with thermal annealing, experimentally observed in Fig. 1(c). Consequently, we next focus on the variation of ω_p and $\mathcal{D}_G(\omega_p)$ with the disorder parameters, in the same physically relevant regime of $y \ll 1$.

To derive scaling relations for ω_p and $\mathcal{D}_G(\omega_p)$ in the small y regime, we need to better understand how $\mathcal{D}_G(\omega)$ emerges from $g_0(\omega)$. First, we note that there exists a frequency scale $\omega_\times \sim h^{1/3}$ such that liquidlike vibrations with $\omega > \omega_\times$ are weakly affected by the disorder parameters h and J, while for $\omega < \omega_\times$ liquidlike vibrations undergo significant modification ("reconstruction"), as shown in Fig. 2(a). Second, the vast majority of the reconstructed vibrations are added on top of $g_0(\omega)$ in the frequency range $[\omega_g,\ \omega_\times]$ [marked by light-blue shading in Fig. 2(a)], where ω_g is also marked therein. These vibrations constitute the peak at ω_p. A small fraction of the reconstructed vibrations populate the frequency range $[0\,,\,\omega_g]$ [marked by light-green shading in Fig. 2(a)], including those in the universal $\sim\omega^4$ tail.

The number of vibrations in the frequency range $[0,\ \omega_\times]$ is conserved upon reconstruction. This, together with neglecting the number of reconstructed vibrations in $[0\,,\,\omega_g]$ compared to those that populate the peak region in $[\omega_g,\ \omega_\times]$, yields (Appendix A 3)

$$\omega_p \sim h^{1/3} \quad \text{and} \quad \mathcal{D}_G(\omega_p) \sim h^{1/3}/\omega_0^2\,. \tag{2}$$

The scaling predictions in Eq. (2) suggest that while $J > 0$ (accounting for interactions between vibrations) is essential for the emergence of the universal $\sim\omega^4$ tail (recall that $A_g \to 0$ as $J \to 0$), it contributes only to subleading orders in the peak properties, in the $y = J/(h^{1/3}\kappa_0^{1/2}) \ll 1$ limit of interest. In Fig. 3, the scaling predictions in Eq. (2) are quantitatively verified by numerical solutions of the mean-field model. Importantly, Eq. (2), along with $A_g \sim \exp(-c_g\kappa_0\, h^{2/3}/J^2)$, indicates that an increase in the disorder parameter h at fixed J gives rise to strong (exponential) reduction in the $\sim\omega^4$ tail, but to weak (power-law) increase in ω_p and $\mathcal{D}_G(\omega_p)$. These predictions are in qualitative agreement with the experimental trends presented in Fig. 1.

IV. NATURE OF THE BOSON PEAK MODES AND THEIR LOCALIZATION PROPERTIES

Up to now, we focused on the VDoS $\mathcal{D}_G(\omega)$ and its properties, but not on the nature of the boson peak vibrational modes themselves, in particular their spatial structure. Current experimental techniques entirely lack the spatial resolution to address this issue, and hence we approach it in the framework of the mean-field model and atomistic computer simulations. In the context of the former, the question boils down to quantifying how many oscillators are taking part in each vibration at minima of the Hamiltonian, i.e., the degree of localization of vibrations, commonly quantified through the averaged

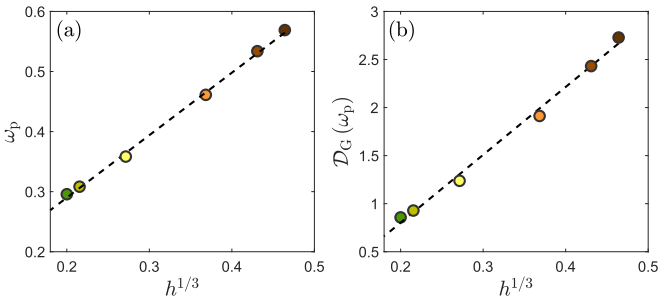

FIG. 3. (a) The prediction $\omega_p \sim h^{1/3}$ of Eq. (2) is verified using numerical solutions of the mean-field model with $J = 0.05$ and $h = [0.1, 0.08, 0.05, 0.02, 0.01, 0.008]$ (recall that $\kappa_0 = 1$), corresponding to small $y = J/(h^{1/3}\kappa_0^{1/2})$ values (between ≈ 0.11 and 0.25). The color corresponds to the different h values. (b) The prediction $\mathcal{D}_G(\omega_p) \sim h^{1/3}$ of Eq. (2) is verified using the same numerical solutions of the mean-field model used in panel (a). The dashed lines are guides to the eye. Note that while ω_p and $\mathcal{D}_G(\omega_p)$ increase by approximately a factor of 2 over the presented range of disorder, A_g decreases by many orders of magnitude (not shown).

participation ratio $\bar{e}(\omega)$ (Appendix A 4). A vibration that is fully localized at a single oscillator features a participation ratio of $1/N$ (recall that N is the total number of oscillators). On the other hand, a fully delocalized vibration features a participation ratio of unity.

In Fig. 2(b), we present $\bar{e}(\omega)$, corresponding to $\mathcal{D}_G(\omega)$ shown in Fig. 2(a). $\bar{e}(\omega)$ attains a peak near ω_p, i.e., $\bar{e}(\omega)$ is peaked in the boson peak region [52]. In addition, Fig. 2(b) shows that $N\bar{e}(\omega_p) \gg 1$, i.e., it suggests that boson peak vibrational modes feature many coupled quasilocalized vibrations, while modes in the $\sim\omega^4$ tail feature $N\bar{e}(\omega_p)$ that is orders of magnitude smaller [40]. Finally, $\bar{e}(\omega)$ plateaus at frequencies above the peak.

The prediction that boson peak vibrational modes feature many coupled quasilocalized vibrations poses serious challenges. Testing it in computer glasses requires tools for identifying quasilocalized vibrations inside boson peak vibrational modes, possibly featuring many hybridized/mixed quasilocalized vibrations and extended phonons [32–34,38]. Such tools have just began to emerge [38,45], and Fig. 4(a) presents a preliminary example [corresponding to Fig. 3(d) in [38]]. As stressed above, we use here an example in two dimensions for visual clarity. The figure shows a superposition of identified quasilocalized vibrations in a boson peak vibrational mode in a two-dimensional computer glass [the full boson peak vibrational mode is shown in Fig. 3(c) in [38]], clearly supporting the prediction of the existence of many coupled quasilocalized vibrations.

We next derive scaling relations for $\bar{e}(\omega)$, shown in Fig. 2(b), in the framework of the mean-field model. In Fig. 4(b), we present $\bar{e}(\omega)$ for several combinations of the disorder parameters J and h (we set $\kappa_0 = 1$, as done elsewhere in this paper), all in the $y = J/(h^{1/3}\kappa_0^{1/2}) \ll 1$ regime of interest. In the $\sim\omega^4$ tail region, vibrations in the mean-field model are rather localized [50], corresponding to the very small observed values of $\bar{e}(\omega \to 0)$ [see Fig. 4(b)]. We do not discuss the tail region here, but rather focus on the peak region and the plateau that follows it.

The averaged participation ratio $\bar{e}(\omega)$ emerges from interactions between the oscillators, mediated by the bilinear coupling coefficients J_{ij}, i.e., one trivially has $N\bar{e}(\omega) = 1$ for $J = 0$. Moreover, since we consider the $y = J/(h^{1/3}\kappa_0^{1/2}) \ll 1$ regime (and set $\kappa_0 = 1$), we can treat the effect of weak

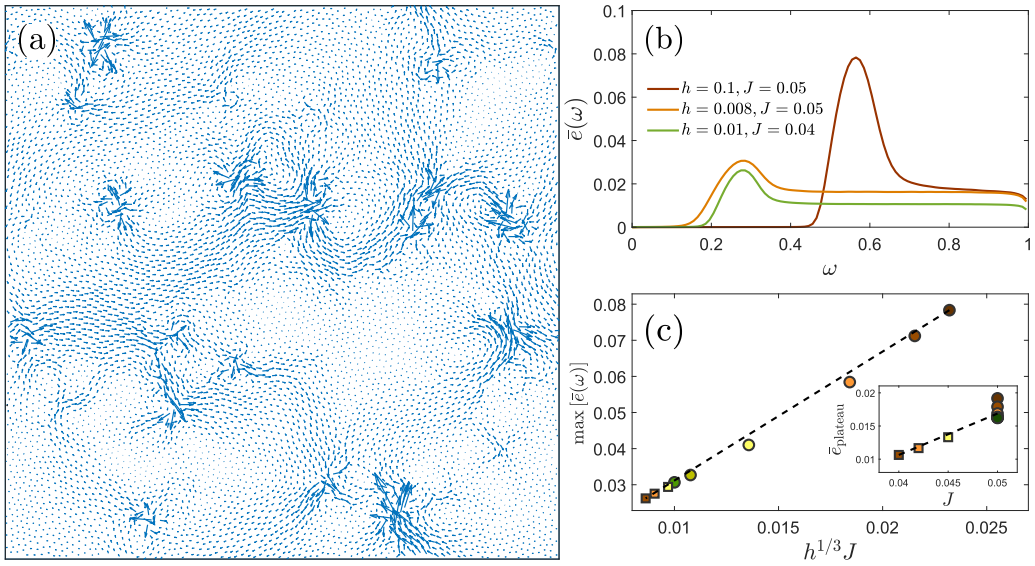

FIG. 4. (a) A superposition of quasilocalized nonphononic vibrations identified inside a boson peak vibrational model in the same canonical computer glass model (in two dimensions) used in Fig. 1 (see [38] for details). (b) The averaged participation ratio $\bar{e}(\omega)$ for a few sets of the disorder parameters (see legend). (c) The prediction $\max[\bar{e}(\omega)] \sim h^{1/3}J$ (see text for details) is verified using numerical solutions of the mean-field model with $J = 0.05$ and $h = [0.1, 0.08, 0.05, 0.02, 0.01, 0.008]$ (circles, the same as in Fig. 3), and with $h = 0.01$ with $J = [0.04, 0.042, 0.045]$ (squares), all corresponding to small $y = J/(h^{1/3}\kappa_0^{1/2})$ values. $\max[\bar{e}(\omega)]$ is the maximum of $\bar{e}(\omega)$, attained very close to ω_p (cf. Fig. 2). Inset: The prediction $\bar{e}_{plateau} \sim J$ (see text for details) is verified using the same numerical solutions as in the main panel (same symbols and colors). $\bar{e}_{plateau}$ corresponds to the plateau value of $\bar{e}(\omega)$, above the maximum. The dashed lines are guides to the eye.

interactions of characteristic size J as perturbations on top of the $J = 0$ and $h > 0$ case. The latter is fully described by the single-oscillator Hamiltonian $\kappa x^2/2 + x^4/24 - hx$, implying that liquidlike vibrations below $\kappa \sim h^{2/3}$ are blueshifted and accumulate in a narrow stiffness range near $\kappa \sim h^{2/3}$, while those above $\kappa \sim h^{2/3}$ are weakly affected (Appendix A 4). When weak random interactions are introduced, $J > 0$, the number of oscillators that contribute to reconstructed vibrations must scale with J to leading order. Near $\omega_p \sim h^{1/3}$, there are $\sim N h^{2/3}$ blueshifted vibrations and hence the participation ratio after reconstruction satisfies $N\bar{e}(\omega_p) \sim \sqrt{N} h^{1/3} J$, implying $\max[\bar{e}(\omega)] \sim h^{1/3} J/\sqrt{N}$.

This scaling prediction is verified in Fig. 4(c) against a numerical solution of the model. It shows that internal stresses, represented by h, and disorder-mediated interactions between the oscillators, represented by the standard deviation $J/\sqrt{N}$ of the random variables J_{ij}, lead to $N\bar{e}(\omega) \gg 1$ near the boson peak. That is, the mean-field model predicts that boson peak modes feature many coupled quasilocalized vibrations (in terms of the oscillators participation ratio), which mirrors the same physical picture demonstrated in space in Fig. 4(a). Moreover, note that $\bar{e}(\omega_p) \sim h^{1/3} J$, together with Eq. (2) (verified in Fig. 3), implies $\bar{e}(\omega_p) \sim \mathcal{D}(\omega_p) J$. Finally, above $\omega_p \sim h^{1/3}$, the stiffnesses are uniformly distributed and weakly affected by h, hence we have $\bar{e}_{\text{plateau}} \sim J/\sqrt{N}$, where $\bar{e}_{\text{plateau}}$ is the plateau level of $\bar{e}(\omega)$ [see Fig. 4(b)]. This prediction is verified in the inset of Fig. 4(c).

Overall, while the mean-field model is not yet quantitatively compared to experimental and simulational data, it appears to offer a physical picture of the low-frequency vibrational spectra of glasses. This emerging physical picture is consistent with all of the trends observed in the experimental and simulational data.

V. SUMMARY AND DISCUSSION

Our results shed basic light on the origin, nature, and properties of the universally observed boson peak in glasses. We followed [15] and showed that the nonphononic part of the VDoS $\mathcal{D}_G(\omega)$ features an intrinsic peak at ω_p, which is distinguished from the conventionally defined peak in the reduced VDoS $\mathcal{D}(\omega)/\omega^2$, commonly denoted by ω_{BP}. Generically, it is observed that $\omega_p > \omega_{BP}$ (Appendix A 1), even though the two frequencies are comparable, both being in the terahertz range. While the definition of ω_{BP} involves Debye's VDoS of phonons, ω_p is an intrinsic property of the nonphononic VDoS. Moreover, our results indicate—at the fundamental ontological level—that the excess vibrations that constitute the boson peak are the very same quasilocalized nonphononic vibrations that populate the universal $\sim\omega^4$ tail of $\mathcal{D}_G(\omega)$, in line with the preliminary recent observations in two-dimensional computer glasses [38].

The latter findings are also consistent with suggestions in earlier modeling efforts [33], which inspired the formulation of the mean-field Hamiltonian in Eq. (1); see discussion in [49,50]. The relations between the predictions of our model in the context of the boson peak and those of [33] are discussed in Appendix B 3 (see Fig. 8 in particular). The differences between the predictions of the models further highlight the importance of extracting the intrinsic properties of the nonphononic VDoS $\mathcal{D}_G(\omega) = \mathcal{D}(\omega) - A_D\,\omega^2$, rather than considering the reduced VDoS $\mathcal{D}(\omega)/\omega^2$, which involves different pieces of physics (i.e., nonphononic and phononic excitations); see Appendix B 3.

We further showed that vibrational modes near the boson peak feature many more coupled quasilocalized nonphononic vibrations than modes in the universal tail. Moreover, the peak frequency ω_p and its magnitude $\mathcal{D}_G(\omega_p)$ mildly increase upon thermal annealing (i.e., with decreasing degree of glassy disorder), while $\mathcal{D}_G(\omega)$ is strongly reduced in the tail region under the same conditions. Taken together, these findings provide a unified picture of the low-frequency properties of the nonphononic VDoS $\mathcal{D}_G(\omega)$. This picture is also expected to be valid in disordered crystals, especially in view of the recent results of [53], an issue that should be further explored in future work.

Future work, both experimental and simulational, should further test these predictions for a broader range of glasses and disordered crystals under different nonequilibrium histories. Future work should also explore the implications of our findings to other glass properties, such as the specific heat, not discussed here. Finally, all of our findings are shown to be in qualitative agreement with a mean-field model of interacting quasilocalized vibrations, which also predicts the universal $\sim\omega^4$ tail of $\mathcal{D}_G(\omega)$. As such, future work should further explore the predictive powers of the model in relation to other properties of glasses.

ACKNOWLEDGMENTS

A.M. acknowledges support from the Minerva center on "Aging, from physical materials to human tissues." E.L. acknowledges support from The Dutch Research Council (Vidi Grant No. 680-47-554/3259). E.B. acknowledges support from the Ben May Center for Chemical Theory and Computation and the Harold Perlman Family.

APPENDIX A: METHODS

1. Reanalysis of thermal annealing experimental data

The data presented in Figs. 1(b) and 1(c) correspond to the experimental data digitized from Fig. 3 in [25], reproduced here in its original form in Fig. 5, and to the values of A_D appearing therein. In Fig. 5 (i.e., Fig. 3 in [25]), the measured VDoS $g(\nu)$ [denoted by $\mathcal{D}(\nu)$ in the paper and obtained as explained in [25], also using the specific heat data of [24]] divided by ν^2 was plotted (ν is the Raman wave-number shift in units of cm^{-1}) for B_2O_3 glass samples of different thermal histories and water content. The different samples were given names and the corresponding data were denoted by different symbols, as indicated in Fig. 5. The names and symbols, from the top curve to the bottom one, are D1 and circles, D3 and down triangles, D5 and up triangles, and W2 and squares. The thermal history and water content of each sample are detailed in Table I.

The D1 sample is termed "as quenched" in the manuscript, D3 is termed "annealed I," and D5 is termed "annealed II." All of these samples do not contain water ("D" stands for "dry"). The W2 sample is termed "most annealed," which is the only wet sample we considered ("W" stands for "wet").

TABLE I. The thermal history (annealing treatment) and water content (dry/wet) of the different B_2O_3 glass samples of [23–25], and all physical quantities that characterize them. The thermal history, except for the as quenched sample, is characterized by the annealing temperature (in Kelvin) and annealing time (in hours) applied to the as quenched sample (see second column). A_D, ρ, and μ are extracted from the existing literature (see text for details), while ν_p and $\mathcal{D}(\nu_p)$ are obtained from Fig. 1(b). ν_{BP}, which is added for completeness, is extracted from the data shown in Fig. 5. The relative variation with annealing of each quantity, relative to the as quenched sample (D1), is reported in brackets in each column.

Symbol	Thermal history	A_D (a.u.)	ν_p (cm^{-1})	$\mathcal{D}_G(\nu_p)$ (a.u.)	ρ (g/cm^3)	μ (GPa)	ν_{BP} (cm^{-1})
D1 (as quenched, dry)	As quenched	1.639 (1)	30.02 (1)	1365.91 (1)	1.804 (1)	6.14 (1)	15.0 (1)
D3 (annealed I, dry)	530 K, 50 h	1.514 (0.92)	30.37 (1.01)	1529.48 (1.12)	1.826 (1.01)	6.52 (1.06)	16.5 (1.10)
D5 (annealed II, dry)	480 K, 170 h	1.417 (0.86)	31.44 (1.05)	1563.07 (1.14)	1.834 (1.02)	6.89 (1.12)	17.5 (1.17)
W2 (most annealed, wet)	490 K, 100 h	1.292 (0.79)	36.16 (1.20)	1520.80 (1.11)	1.866 (1.03)	7.50 (1.22)	19.0 (1.27)

B_2O_3 glasses are hygroscopic and water inclusion tends to rigidify them. Consequently, while the W2 sample is roughly as annealed as the D5 sample in terms of thermal annealing, it is the densest and hence effectively the most annealed sample [see the density column in Table I, but note that the peak value, $\mathcal{D}_G(\nu_p)$, is a bit reduced due to the effect of water on the material].

We also follow the same symbols scheme in Figs. 1(b) and 1(c), except that we replaced the down triangles for the D3 sample data by diamonds for improved visual clarity (as well as colors). We digitized the data for $g(\nu)/\nu^2$ shown in Fig. 5 and multiplied it by ν^2 to obtain $\mathcal{D}(\nu) = g(\nu)$. The horizontal solid lines in Fig. 5 correspond to the values of A_D for each sample, which we digitized as well; the values are also reported in Table I. We then plotted the nonphononic VDoS $\mathcal{D}_G(\nu) \equiv \mathcal{D}(\nu) - A_D\,\nu^2$ in Figs. 1(b) and 1(c).

The position of the peak of $\mathcal{D}_G(\nu)$, denoted by ν_p, is reported in Table I for the different thermal histories and water content, as well as the peak value, $\mathcal{D}_G(\nu_p)$. For completeness, we added in Table I the mass density ρ of each sample (extracted from Table 1 of [25]). Moreover, we used Debye's velocity values v_d from [25], together with the longitudinal (dilatational) wave speed v_l values from [23], to extract the transverse (shear) wave speed v_t using the relation $3v_d^{-3} = v_l^{-3} + 2v_t^{-3}$ [23]. Then, we used the density ρ to extract the shear modulus $\mu = \rho\, v_t^2$, as reported in Table I. The obtained μ values are consistent with those of [54]. To highlight the variability of all physical quantities with annealing and water inclusion, we added to each column in Table I the relative variation with respect to the as quenched sample (in brackets).

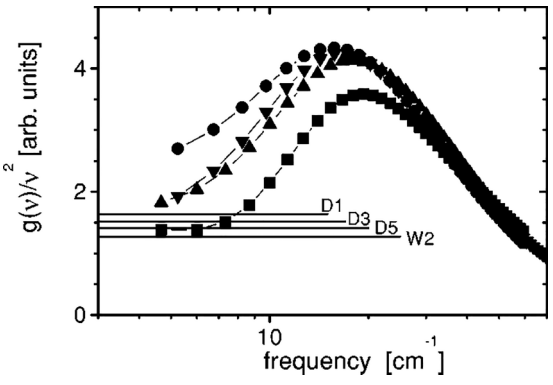

FIG. 5. The experimental data of [25], adapted as originally reported in Fig. 3 therein. See text for extensive discussion. Note that the variation (with annealing and water content) of the properties of the peak—i.e., its frequency ν_{BP} and magnitude—in the conventional reduced-VDoS presentation is just opposite to the variation shown in Fig. 1(b), using the nonphononic VDoS $\mathcal{D}_G(\nu)$. Similar qualitative differences associated with the two presentations were highlighted in [15,16].

Finally, we add for completeness the conventional ν_{BP} to Table I, as extracted from the data shown in Fig. 5. It is observed that ν_{BP} is smaller than ν_p due to the division by the phononic ν^2 VDoS. This is theoretically expected since ν_{BP} is the solution of $d[\mathcal{D}(\nu)/\nu^2]/d\nu = 0$, implying $\mathcal{D}'_G(\nu_{BP}) = 2\mathcal{D}_G(\nu_{BP})/\nu_{BP} > 0$ [recall that $\mathcal{D}(\nu)/\nu^2 = \mathcal{D}_G(\nu)/\nu^2 + A_D$ based on the additive decomposition $\mathcal{D}(\nu) = \mathcal{D}_G(\nu) + A_D\nu^2$]. On the other hand, ν_p is determined by $\mathcal{D}'_G(\nu_p) = 0$. Since $\mathcal{D}_G(\nu)$ is an increasing function for $\nu < \nu_p$, we obtain $\nu_{BP} < \nu_p$. In quantitative terms, the two frequencies are comparable (within a factor of 2 for these data), both being in the terahertz range.

We note that both the conventional reduced VDoS $D(\nu)/\nu^2$ and the additive decomposition for extracting the nonphononic VDoS $D_G(\nu)$, $\mathcal{D}_G(\nu) = \mathcal{D}(\nu) - A_D\nu^2$ assume that Debye's VDoS $\mathcal{D}(\nu) = A_D\nu^2$ of phonons extends to frequencies above the estimated boson peak in both procedures. In view of the relation $\nu_{BP} < \nu_p$, one should be even more aware of this issue—and the possible quantitative uncertainties involved (for a given material)—in relation to the additive decomposition procedure.

2. Atomistic computer glasses

We employ a simple glass-forming model in three dimensions [55] in which half of the particles are "large" and half are "small." The particles of both species have equal mass m. The pairwise potential of this model is given by

$$\varphi(r,\lambda)/\varepsilon = \left(\frac{\lambda}{r}\right)^{10} + \sum_{\ell=0}^{3} c_{2\ell}\left(\frac{r}{\lambda}\right)^{2\ell}, \qquad \text{(A1)}$$

where ε denotes our microscopic units of energy, r is the pairwise distance between two particles, and $c_{2\ell}$ are coefficients (reported in Table II below) that guarantee the smoothness of the potential at the dimensionless cutoff distance $r_c = 1.48\lambda$, where $\lambda = 1.4\text{Å}$ for large-large pairs, $\lambda = 1.18\text{Å}$ for large-small pairs, and $\lambda = 1.0\text{Å}$ for small-small pairs. Å denotes the microscopic units of length. We fix the number density at

TABLE II. The coefficients $c_{2\ell}$ appearing in Eq. (A1).

Parameter	Value
c_0	−1.1106337662511798
c_2	1.2676152372297065
c_4	−0.4960406072849212
c_6	0.0660511826415732

$N/V = 0.82$ for all simulations (N denotes the total number of particles and V denotes the volume). All dimensional observables reported in the paper should be understood as expressed in terms of the aforementioned microscopic units m, ε, and $\lambda\!\!\!^{-}$.

We prepared glassy samples following two protocols; for both protocols, we first equilibrate high temperature liquid states at $T = 1.0$. Then, in the first protocol, we perform an instantaneous quench (hyperquench) using a standard conjugate gradient minimization algorithm, corresponding to an infinite quench rate $\dot{T} \to \infty$. In the second protocol, we cool the system at a finite cooling rate $\dot{T} = 10^{-3}$, removing any remnant heat deep in the glass phase with a potential-energy minimization. Using these two glass-formation protocols, we prepared 40 independent realizations of $N = 4 \times 10^6$ particles.

VDoS calculations

The VDoS of large computer glasses of several million particles can be obtained using the *kernel polynomial method* (KPM) [56]. We followed exactly the procedure as described in detail in [57]. The KPM requires choosing the *truncation degree* K, and the number R of initial random vectors used in the calculation. We chose $K = 3000$ and $R = 10$, in addition to carrying out this analysis over 40 independent glasses.

3. Mean-field model: Numerical solutions and scaling relations for $\mathcal{D}_{\rm G}(\omega)$

The main properties of the nonphononic VDoS $\mathcal{D}_{\rm G}(\omega)$ in the framework of the mean-field model, defined in Eq. (1) are extensively discussed in the paper. Here, we provide details of the numerical solution procedure and some supporting results in relation to the scaling predictions discussed in the paper.

Numerical solutions for the statistics of energy minima of the Hamiltonian in Eq. (1) in the paper are obtained as follows. We initiated $M = 2000$ different realizations of $N = 16\,000$ coupled oscillators each. The initial oscillators' positions $x_i^{(0)}$ were set randomly in the range $x_i^{(0)} \in [-0.005, 0.005]$. These initial positions generate nonvanishing net forces on the oscillators. After initiation, we used a gradient descent algorithm to relax the oscillators to the closest mechanically stable energy minimum, resulting in displacements x_i. Following this minimization procedure, we calculated the Hessian matrix $\mathcal{M}_{ij} \equiv \frac{\partial^2 H}{\partial x_i \partial x_j}$ at this newly attained energy minimum, and diagonalized it to find the eigenmodes $\boldsymbol{\psi}$ and their corresponding eigenvalues ω^2, according to $\boldsymbol{\mathcal{M}} \cdot \boldsymbol{\psi} = \omega^2 \boldsymbol{\psi}$ ($\boldsymbol{\psi}$ is normalized, $\sum_i |\psi_i|^2 = 1$). $\mathcal{D}_{\rm G}(\omega)$ is obtained by generating a histogram over the vibrational frequencies collected from all realizations, as presented in Fig. 2(a). This procedure was repeated for every pair of J and h values.

As we exclusively focused on the $y \equiv J/(h^{1/3}\kappa_0^{1/2}) \ll 1$ regime, we followed [49] and treated the characteristic interactions strength J as a small perturbation on top of the characteristic internal force h. It was shown in [49] that there exists a characteristic frequency scale $\omega_\times$ that splits the entire frequency domain $[0, \omega_0]$ into two parts, one in which the VDoS undergoes "reconstruction," $0 < \omega < \omega_\times$, and another in which it mostly does not, $\omega_\times < \omega < \omega_0$. The scaling prediction for $\omega_\times$ takes the form $\omega_\times \sim h^{1/3}(1 + c_\times y)$ [49], where the two leading orders in y are included (note that in the paper only the leading order $\omega_\times \sim h^{1/3}$ is discussed).

Focusing on the reconstructed domain $0 < \omega < \omega_\times$, we considered the frequency $\omega_{\rm g}$ defined according to the lowest $\omega > 0$ solution to $\mathcal{D}_{\rm G}(\omega) = g_0(\omega)$ [see Fig. 2(a)]. Modes below $\omega_{\rm g}$ are blueshifted (by amount $\sim h^{1/3}$) to the frequency domain $\omega_{\rm g} < \omega < \omega_\times$ (see [49] and Fig. 7). A tiny fraction of these blueshifted modes are "pushed back" to the frequency domain $0 < \omega < \omega_{\rm g}$ by interaction-induced fluctuations, forming the gapless (or pseudogapped) $\mathcal{D}_{\rm G}(\omega) = A_{\rm g}\,\omega^4$ tail. The latter implies $\int_0^{\omega_{\rm g}} \mathcal{D}_{\rm G}(\omega)\,d\omega \ll \omega_{\rm g}^2/\omega_0^2$. Since the reconstruction of $\mathcal{D}_{\rm G}(\omega)$ in the frequency domain $0 < \omega < \omega_\times$ only redistributes the modes, conservation of modes then implies

$$\int_{\omega_{\rm g}}^{\omega_\times} [\mathcal{D}_{\rm G}(\omega) - g_0(\omega)]d\omega \simeq \omega_{\rm g}^2/\omega_0^2\,, \tag{A2}$$

which is verified in Fig. 6(a).

The validity of Eq. (A2) justifies neglecting the light-green-shaded area in Fig. 2(a) compared to the light-blue-shaded area therein, as done in the paper. In addition, we estimate $\int_{\omega_{\rm g}}^{\omega_\times} \mathcal{D}_{\rm G}(\omega)\,d\omega$ as $\mathcal{D}_{\rm G}(\omega_\times)(\omega_\times - \omega_{\rm g})$, which implies $\omega_{\rm g} \sim \omega_\times \sim h^{1/3}$ to leading order in small y. This prediction is verified in Fig. 6(b). Since scalingwise we have $\omega_{\rm p} \sim (\omega_{\rm g} + \omega_\times)/2$, we end up with

$$\omega_{\rm p} \sim \omega_{\rm g} \sim \omega_\times \sim h^{1/3}(1 + c_\times y)\,, \tag{A3}$$

which is verified in Fig. 6(c). Finally, by estimating Eq. (A2) as $\int_{\omega_{\rm g}}^{\omega_\times} [\mathcal{D}_{\rm G}(\omega) - g_0(\omega)]d\omega \simeq [\mathcal{D}_{\rm G}(\omega_{\rm p}) - 2\omega_{\rm p}/\omega_0^2](\omega_\times - \omega_{\rm g}) \sim \omega_{\rm g}^2/\omega_0^2$, Eq. (2) is obtained.

4. Mean-field model: The average participation ratio $\bar{e}(\omega)$

The averaged participation ratio $\bar{e}(\omega)$ and its scaling properties are extensively discussed in the paper. Here, we provide the relevant definition, the numerical averaging procedure, and some supporting data referred to in the paper.

The participation ratio of an eigenmode $\boldsymbol{\psi}^{(\rm j)}$, which is a normalized solution to $\boldsymbol{\mathcal{M}} \cdot \boldsymbol{\psi}^{(\rm j)} = [\omega^{(\rm j)}]^2\,\boldsymbol{\psi}^{(\rm j)}$ (i.e., $\sum_i |\psi_i^{(\rm j)}|^2 = 1$), is defined as

$$e^{(\rm j)} \equiv \frac{1}{N \sum_{i=1}^N \left[\psi_i^{(\rm j)}\right]^4} \tag{A4}$$

where the index i corresponds to the projection on the ith oscillator. Finding the complete set of eigenmodes $\boldsymbol{\psi}^{(\rm j)}$ per realization of the disorder (with fixed J, h, and κ_0), we sort $e^{(\rm j)}$ according to their corresponding frequencies $\omega^{(\rm j)}$, collect data from all M realizations, and average over bins of size $\Delta\omega$

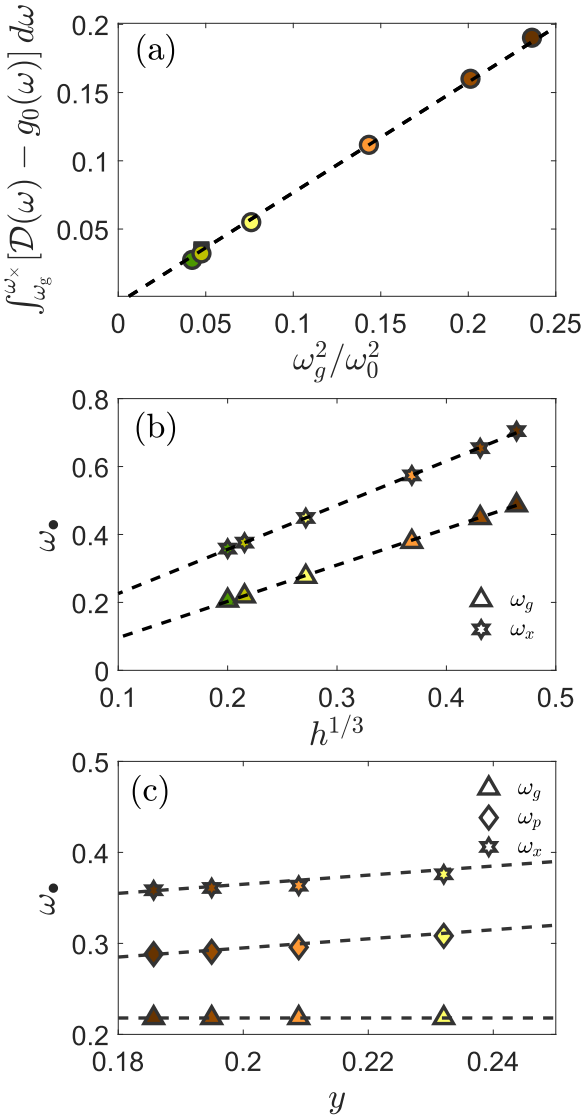

FIG. 6. (a) Verification of Eq. (A2). Circles correspond to fixed $J = 0.05$ with $h = [0.1, 0.08, 0.05, 0.02, 0.01, 0.008]$ and squares correspond to fixed $h = 0.01$ with $J = [0.04, 0.042, 0.045]$. We used $\omega_0 = 1$ as done throughout this paper. (b) Verification of the $\sim h^{1/3}$ scaling of ω_g and $\omega_\times$ (see text) for $J = 0.05$ and $h = [0.1, 0.08, 0.05, 0.02, 0.01, 0.008]$. The corresponding prediction for ω_p is verified in Fig. 3(a). (c) Verification of the subleading (linear) contribution in y in the prediction $\omega_\bullet \sim h^{1/3}(1 + c_\times y)$ for ω_g, ω_p, and $\omega_\times$, for fixed $h = 0.01$ with $J = [0.04, 0.042, 0.045, 0.05]$.

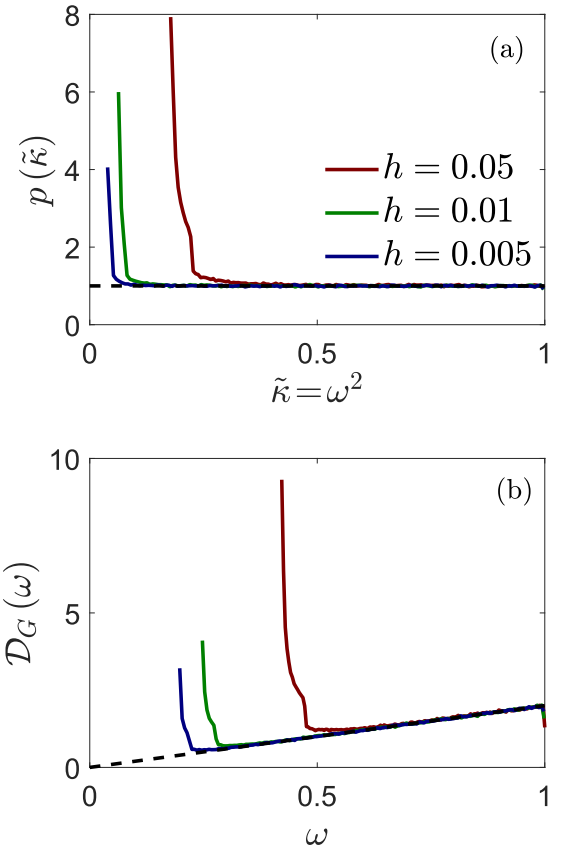

FIG. 7. (a) The transformation of the initial liquidlike distribution $p(\kappa) = \kappa_0^{-1}$ (for $0 \leqslant \kappa \leqslant \kappa_0$, with $\kappa_0 = 1$) into $p(\tilde{\kappa})$ upon the introduction of internal stresses represented by $h > 0$, in the absence of interactions between oscillators, $J = 0$ (i.e., when the single-oscillator Hamiltonian reads $\kappa x^2/2 + x^4/24 - hx$). $p(\tilde{\kappa})$ is plotted for three values of h (indicated in the legend), revealing a gap that increases as $\sim h^{2/3}$ and leads to the accumulation of $\sim N h^{2/3}$ blueshifted oscillators in a narrow stiffness range near $\tilde{\kappa} \sim h^{2/3}$. Note that $\tilde{\kappa} = \omega^2$ (as indicated in the x-axis label) and that the corresponding distribution for ω is shown in panel (b) for completeness. (b) The same as panel (a), but for the frequency ω. That is, $\mathcal{D}_G(\omega)$ for the noninteracting case of $J = 0$ and $h > 0$ is shown.

to obtain $\bar{e}(\omega)$. That is, we define

$$\bar{e}(\omega) \equiv \langle e(\omega) \rangle_{\omega,\omega+\Delta\omega}\,, \tag{A5}$$

where $\langle \bullet \rangle_{\omega,\omega+\Delta\omega}$ denotes averaging over modes with frequencies in the range $[\omega, \omega + \Delta\omega]$. In particular, we used $\Delta\omega = 0.01$ to produce the averaged participation ratio curves in Figs. 2(b) and 4. In the paper, the main scaling predictions for $\bar{e}(\omega)$—i.e., $\bar{e}(\omega_p) \sim h^{1/3} J$ and $\bar{e}_{\text{plateau}} \sim J$—are derived using a perturbative approach in which the $J = 0$ and $h > 0$ case is considered first, and then weak interactions $J > 0$ are considered. It is stated therein that for $J = 0$ and $h > 0$ (described by the noninteracting single-oscillator Hamiltonian $\kappa x^2/2 + x^4/24 - hx$), the liquidlike vibrations below $\kappa \sim h^{2/3}$ are blueshifted and accumulate in a narrow stiffness range near $\kappa \sim h^{2/3}$, while those above $\kappa \sim h^{2/3}$ are weakly affected. This is explicitly demonstrated in Fig. 7.

APPENDIX B: ADDITIONAL INFORMATION AND SUPPORTING RESULTS

1. Thermal history variability of various physical quantities

The experimental results summarized in Table I demonstrate the annealing and water content variability of various basic physical quantities. It is observed that Debye's prefactor A_D decreases with annealing, which mostly reflects the stiffening of the elastic moduli. Indeed, the shear modulus μ increases with annealing (by 22% between the most annealed and as quenched samples). As discussed extensively in this paper, both ν_p and $\mathcal{D}_G(\nu_p)$ mildly increase with annealing. Finally, samples undergo densification (i.e., increase of the

TABLE III. The symbols of the different computer glass samples and the physical quantities that characterize them. The thermal history is characterized by the quench rate used (see the "Thermal history" column). μ is directly computed, and $A_D = 3/\omega_D^3$. ω_p and $\mathcal{D}_G(\omega_p)$ are extracted from Fig. 1(d). Since the simulations are performed at a fixed volume, we report the hydrostatic pressure p of the glasses (the counterpart of the density ρ in Table I). The variation of each quantity, relative to the $\dot{T} = \infty$ samples, is reported in brackets in each column.

Thermal history	A_D	ω_p	$\mathcal{D}_G(\omega_p)$	p	μ
$\dot{T} = \infty$	6.9×10^{-4} (1)	4.15 (1)	0.0075 (1)	18.88 (1)	12.75 (1)
$\dot{T} = 10^{-3}$	5.8×10^{-4} (0.85)	4.89 (1.18)	0.009 (1.2)	18.67 (0.99)	14.25 (1.12)

mass density ρ) with annealing and water inclusion. Note in this context that the experiments are done under NPT conditions (constant pressure) such that the thermal history affects the volume.

It would be interesting to consider also the covariation of various physical quantities. The frequency scale ν_p that is associated with the peak of $\mathcal{D}_G(\nu)$ defines a stiffness scale $\sim\nu_p^2$. The latter characterizes the stiffness of quasilocalized vibrations in the boson peak region, i.e., it is a mesoscopic elastic response coefficient. According to Table I, ν_p^2 increases (stiffens) by 45% (obtained from $(36.16/30.02)^2$) between the most annealed and as quenched samples. It would be natural and interesting to compare this observation to the annealing variability of the macroscopic elastic coefficient, i.e., the shear modulus μ. Previous work indicated that the degree of stiffening with annealing of μ is smaller compared to that of the mesoscopic elastic coefficient associated with quasilocalized vibrations [55,58,59]. Indeed, the annealing variability of μ in the experimental data summarized in Table I is 22%, a factor of 2 smaller than that of ν_p^2, as expected. These experimental observations are also consistent with the ideas and analysis of [60].

The thermal history variability of $\mathcal{D}_G(\omega)$ in the computer glass data, presented in Figs. 1(d) and 1(e), bears close resemblance to the corresponding experimental data, presented in Figs. 1(b) and 1(c). In Table III, we provide the actual values of the peak's location ω_p and its magnitude $\mathcal{D}_G(\omega_p)$, along with Debye's prefactor $A_D = 3/\omega_D^3$, the hydrostatic pressure p, and the shear modulus μ. A_D is obtained using Debye's frequency ω_D, computed using $\omega_D^3 = \frac{18\pi^2\rho_N}{2v_t^{-3}+v_l^{-3}}$, where ρ_N is the number density (to be distinguished from the mass density ρ). Here, $v_t = \sqrt{\mu/\rho}$ is the transverse (shear) wave speed and $v_l = \sqrt{(K + \frac{4}{3}\mu)/\rho}$ is the longitudinal (dilatational) wave speed, where K is the bulk modulus. Note that the simulations are done under NVT conditions (constant volume) such that the thermal history affects the pressure p, which we reported instead of the fixed mass density ρ.

The relative thermal history variability of the various physical quantities in Table III is reported in brackets in each column. These values make it easy to compare the relative thermal variability of various quantities in computer glasses presented in Table III to their experimental counterparts in Table I. The comparison reveals that despite the differences in composition and underlying interaction potential, and despite the different thermal history protocols (variable annealing in the experiments and variable quench rate in the computer simulations), the similarities in the nonphononic VDoS observed in Fig. 1 are semiquantitatively echoed in the two tables.

2. Thermal history variability of dimensionless quantifiers of mechanical disorder

Computer glass simulations, in view of their atomistic resolution, provide access to physical quantities that are currently not accessible experimentally. In recent years, several dimensionless quantifiers of mechanical disorder in glasses have been developed and substantiated [61–64]. These dimensionless quantifiers allow one to put on equal footing different glasses and compare their degree of mechanical disorder. It would therefore be useful to report the values of these dimensionless quantifiers for the computer glasses that have been compared to experiments in the previous subsection.

To that aim, we prepared ensembles of a few thousand glass samples of a few thousand particles each. These are needed for statistical convergence and were used to compute three dimensionless quantifiers of mechanical disorder, as reported next. The first quantifier—studied and discussed in detail in [61,62]—captures the sample-to-sample fluctuations of the macroscopic shear modulus μ; it is defined as

$$\chi \equiv \sqrt{N}\frac{\mathrm{STD}(\mu)}{\mathrm{MEAN}(\mu)}, \tag{B1}$$

where the standard deviation and mean appearing above refer to *ensemble* averages. We find $\chi(\dot{T} = 10^{-3}) \approx 2.6$ and $\chi(\dot{T} = \infty) \approx 3.9$ (see [62] for a comparison of these values with a wide variety of disordered solids).

The second quantifier is the ratio of the nonaffine contribution to the shear modulus that emerges due to glasses' structural disorder/frustration [63,64], and the total shear modulus, namely μ_{na}/μ. Detailed definitions of μ_{na} and μ can be found, e.g., in [63,64], and some representative values of generic computer glasses can be found in [53]. We find $\mu_{na}/\mu \approx 1.05$ for our $\dot{T} = 10^{-3}$ ensembles, and $\mu_{na}/\mu \approx 1.32$ for our hyperquenched $\dot{T} = \infty$ samples.

The third and last dimensionless quantifier of mechanical disorder we report for our computer glasses is the product $A_g\,\omega_\star^5$, where A_g is the prefactor of the $\sim\omega^4$ scaling regime of the nonphononic VDoS, and $\omega_\star \equiv v_t/a_0$ is a characteristic elastic frequency. Here, $a_0 \equiv (V/N)^{1/3}$ is a characteristic interparticle distance. Typical values for the product $A_g\,\omega_\star^5$ can be found in, e.g., [46,53,59,62]. Here, we find $A_g\,\omega_\star^5 \approx 0.50$ for our $\dot{T} = 10^{-3}$ ensembles, and $A_g\,\omega_\star^5 \approx 1.35$ for our hyperquenched $\dot{T} = \infty$ samples.

3. Comparison to the GPS model

In order to highlight additional aspects of the theoretical predictions of our model in relation to the boson peak in glasses, we compare its predictions to the model originally

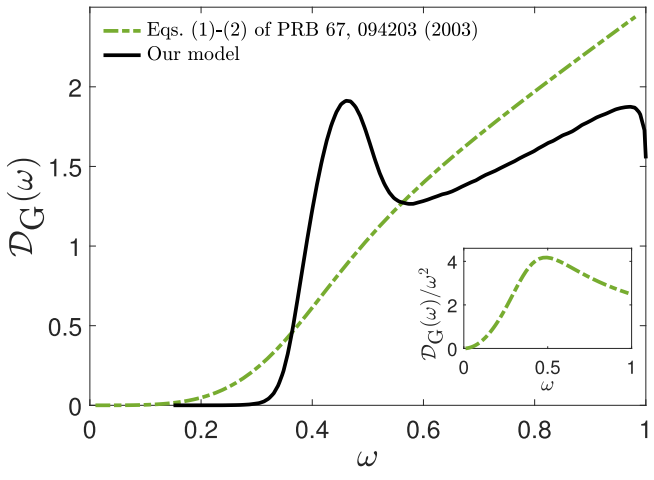

FIG. 8. The nonphononic VDoS $\mathcal{D}_G(\omega)$ of the GPS model in [33] (green dashed-dotted line). It is obtained by multiplying $g(\omega)/\omega^2$ of Eqs. (1) and (2) in [33] by ω^2 and setting $\omega^\star = 0.45$ [$\omega^\star$ is the only parameter therein, not to be confused with $\omega_\star$ of the previous subsection, and the overall amplitude C is selected such that $\mathcal{D}_G(\omega)$ is normalized over the plotted range, $0 \leqslant \omega \leqslant 1$]. For comparison, the corresponding prediction of our model is superimposed (solid black line), revealing a qualitative difference between the two (see text for discussion). Inset: $\mathcal{D}_G(\omega)/\omega^2$ using $\mathcal{D}_G(\omega)$ in the green dashed-dotted line in the main panel. See also Fig. 1 in [33] and text for discussion.

presented in [33], termed the GPS model after its originators. This model, along with the model of [51], inspired the formulation of the model we studied, recently introduced in [49,50]. The GPS model assumes the existence of localized anharmonic vibrations/oscillators that are embedded in three dimensions, which feature $1/r_{ij}^3$ interactions (r_{ij} is the distance between pairs of oscillators with indices i and j) of random amplitudes J_{ij}.

The main difference compared to our model is not dimensionality—our mean-field model formulated in the Hamiltonian of Eq. (1) is infinite dimensional—but rather the existence of finite internal stresses, encapsulated in the term $-h\,x_i$ per oscillator in Eq. (1), which breaks the $x_i \to -x_i$ symmetry of the Hamiltonian. The finite h allowed us to identify a regime of weak interactions, quantified by $y \equiv J/(h^{1/3}\kappa_0^{1/2}) \ll 1$, where the prefactor of the ω^4 tail of the nonphononic VDoS, A_g, features an exponential variation of $-y^{-2}$, as mentioned above [49,50]. This regime does not exist in the GPS model, though the universal tail $\sim\omega^4$ does exist therein in the $\omega \to 0$ limit [33].

Here, we are not interested in the asymptotic tail, $\omega \to 0$, but rather in the boson peak regime, which exists at significantly higher frequencies. The prediction of the GPS model for the nonphononic VDoS $\mathcal{D}_G(\omega)$ is provided in Eqs. (1) and (2) in [33], where it is denoted as $g(\omega)$. We plot $\mathcal{D}_G(\omega)$ corresponding to Eqs. (1) and (2) in [33] in Fig. 8 (green dashed-dotted line). The striking observation is that $\mathcal{D}_G(\omega)$ of the GPS model is a monotonically increasing function of ω, with no peak (local maximum) at all. This is in sharp contrast to the simulational and experimental observations presented in Fig. 1, and the prediction of our model. The latter, a representative example of which is added to Fig. 8 (black solid line), features a peak, similarly to simulational and experimental observations, as discussed extensively above.

Only when $\mathcal{D}_G(\omega)$ of the GPS model is divided by Debye's scaling $\mathcal{D}_D(\omega) \sim \omega^2$, $\mathcal{D}_G(\omega)/\omega^2$, a peak emerges, as demonstrated in the inset of Fig. 8, originally presented in Fig. 1 of [33] [note that conventionally the total VDoS $\mathcal{D}(\omega)$ is used in such boson peak plots, as discussed above]. This result not only highlights yet another important difference between our predictions and those of the GPS model, but also demonstrates the importance of the subtraction procedure of $\mathcal{D}_G(\omega) = \mathcal{D}(\omega) - A_D\,\omega^2$ in revealing the intrinsic properties of the nonphononic VDoS $\mathcal{D}_G(\omega)$. In particular, it shows that dividing two functions, each corresponding to different pieces of physics (i.e., nonphononic and phononic VDoS), can generate a peak, even if the nonphononic part does not feature an intrinsic peak itself.

[1] T. C. Hufnagel, C. A. Schuh, and M. L. Falk, Deformation of metallic glasses: Recent developments in theory, simulations, and experiments, Acta Mater. **109**, 375 (2016).

[2] M. D. Ediger, Perspective: Highly stable vapor-deposited glasses, J. Chem. Phys. **147**, 210901 (2017).

[3] A. Nicolas, E. E. Ferrero, K. Martens, and J.-L. Barrat, Deformation and flow of amorphous solids: Insights from elastoplastic models, Rev. Mod. Phys. **90**, 045006 (2018).

[4] G. Parisi, P. Urbani, and F. Zamponi, *Theory of Simple Glasses: Exact Solutions in Infinite Dimensions* (Cambridge University Press, New York, 2020).

[5] M. A. Ramos, Low-temperature specific heat of glasses and disordered crystals, in *Low-Temperature Thermal and Vibrational Properties of Disordered Solids: A Half-Century of Universal "Anomalies" of Glasses* (World Scientific, Singapore, 2023), pp. 21–67.

[6] A. Cavagna, Supercooled liquids for pedestrians, Phys. Rep. **476**, 51 (2009).

[7] R. C. Zeller and R. O. Pohl, Thermal conductivity and specific heat of noncrystalline solids, Phys. Rev. B **4**, 2029 (1971).

[8] W. Phillips, Tunneling states in amorphous solids, J. Low Temp. Phys. **7**, 351 (1972).

[9] P. W. Anderson, B. I. Halperin, and C. M. Varma, Anomalous low-temperature thermal properties of glasses and spin glasses, Philos. Mag. **25**, 1 (1972).

[10] U. Buchenau, Y. M. Galperin, V. L. Gurevich, D. A. Parshin, M. A. Ramos, and H. R. Schober, Interaction of soft modes and sound waves in glasses, Phys. Rev. B **46**, 2798 (1992).

[11] R. O. Pohl, X. Liu, and E. Thompson, Low-temperature thermal conductivity and acoustic attenuation in amorphous solids, Rev. Mod. Phys. **74**, 991 (2002).

[12] D. Richard, E. Lerner, and E. Bouchbinder, Brittle-to-ductile transitions in glasses: Roles of soft defects and loading geometry, MRS Bull. **46**, 902 (2021).

[13] G. Szamel and E. Flenner, Microscopic analysis of sound attenuation in low-temperature amorphous solids reveals quantitative

importance of non-affine effects, J. Chem. Phys. **156**, 144502 (2022).
[14] C. Kittel, *Introduction to Solid State Physics* (Wiley, New York, 2005).
[15] S. Yannopoulos, K. Andrikopoulos, and G. Ruocco, On the analysis of the vibrational boson peak and low-energy excitations in glasses, J. Non-Cryst. Solids **352**, 4541 (2006).
[16] A. Kalampounias, S. Yannopoulos, and G. Papatheodorou, A low-frequency Raman study of glassy, supercooled and molten silica and the preservation of the boson peak in the equilibrium liquid state, J. Non-Cryst. Solids **352**, 4619 (2006).
[17] B. S. Hudson, Vibrational spectroscopy using inelastic neutron scattering: Overview and outlook, Vib. Spectrosc. **42**, 25 (2006).
[18] W. H. Weber and R. Merlin, *Raman Scattering in Materials Science* (Springer, New York, 2000).
[19] V. Malinovsky and A. Sokolov, The nature of boson peak in Raman scattering in glasses, Solid State Commun. **57**, 757 (1986).
[20] U. Buchenau, Y. M. Galperin, V. L. Gurevich, and H. R. Schober, Anharmonic potentials and vibrational localization in glasses, Phys. Rev. B **43**, 5039 (1991).
[21] M. A. Ramos, S. Vieira, F. J. Bermejo, J. Dawidowski, H. E. Fischer, H. Schober, M. A. González, C. K. Loong, and D. L. Price, Quantitative assessment of the effects of orientational and positional disorder on glassy dynamics, Phys. Rev. Lett. **78**, 82 (1997).
[22] A. Wischnewski, U. Buchenau, A. J. Dianoux, W. A. Kamitakahara, and J. L. Zarestky, Neutron scattering analysis of low-frequency modes in silica, Philos. Mag. B **77**, 579 (1998).
[23] N. Surovtsev, J. Wiedersich, A. Batalov, V. Novikov, M. Ramos, and E. Rössler, Inelastic light scattering in B_2O_3 glasses with different thermal histories, J. Chem. Phys. **113**, 5891 (2000).
[24] E. Pérez-Enciso, M. A. Ramos, and S. Vieira, Low-temperature specific heat of different B_2O_3 glasses, Phys. Rev. B **56**, 32 (1997).
[25] N. V. Surovtsev, A. P. Shebanin, and M. A. Ramos, Density of states and light-vibration coupling coefficient in B_2O_3 glasses with different thermal history, Phys. Rev. B **67**, 024203 (2003).
[26] G. Parisi, On the origin of the boson peak, J. Phys.: Condens. Matter **15**, S765 (2003).
[27] M. Wyart, S. R. Nagel, and T. A. Witten, Geometric origin of excess low-frequency vibrational modes in weakly connected amorphous solids, Europhys. Lett. **72**, 486 (2005).
[28] A. Monaco, A. I. Chumakov, Y.-Z. Yue, G. Monaco, L. Comez, D. Fioretto, W. A. Crichton, and R. Rüffer, Density of vibrational states of a hyperquenched glass, Phys. Rev. Lett. **96**, 205502 (2006).
[29] G. Baldi, A. Fontana, and G. Monaco, Vibrational dynamics of non-crystalline solids, in *Low-Temperature Thermal and Vibrational Properties of Disordered Solids: A Half-Century of Universal "Anomalies" of Glasses* (World Scientific, Singapore, 2023), pp. 177–226.
[30] A. Marruzzo, W. Schirmacher, A. Fratalocchi, and G. Ruocco, Heterogeneous shear elasticity of glasses: The origin of the boson peak, Sci. Rep. **3**, 1407 (2013).
[31] E. DeGiuli, A. Laversanne-Finot, G. During, E. Lerner, and M. Wyart, Effects of coordination and pressure on sound attenuation, boson peak and elasticity in amorphous solids, Soft Matter **10**, 5628 (2014).
[32] H. R. Schober and C. Oligschleger, Low-frequency vibrations in a model glass, Phys. Rev. B **53**, 11469 (1996).
[33] V. L. Gurevich, D. A. Parshin, and H. R. Schober, Anharmonicity, vibrational instability, and the boson peak in glasses, Phys. Rev. B **67**, 094203 (2003).
[34] D. A. Parshin, H. R. Schober, and V. L. Gurevich, Vibrational instability, two-level systems, and the boson peak in glasses, Phys. Rev. B **76**, 064206 (2007).
[35] A. I. Chumakov, G. Monaco, A. Monaco, W. A. Crichton, A. Bosak, R. Rüffer, A. Meyer, F. Kargl, L. Comez, D. Fioretto, H. Giefers, S. Roitsch, G. Wortmann, M. H. Manghnani, A. Hushur, Q. Williams, J. Balogh, K. Parliński, P. Jochym, and P. Piekarz, Equivalence of the boson peak in glasses to the transverse acoustic van hove singularity in crystals, Phys. Rev. Lett. **106**, 225501 (2011).
[36] V. Lubchenko and P. G. Wolynes, The origin of the boson peak and thermal conductivity plateau in low-temperature glasses, Proc. Natl. Acad. Sci. USA **100**, 1515 (2003).
[37] Y.-C. Hu and H. Tanaka, Origin of the boson peak in amorphous solids, Nat. Phys. **18**, 669 (2022).
[38] E. Lerner and E. Bouchbinder, Boson-peak vibrational modes in glasses feature hybridized phononic and quasilocalized excitations, J. Chem. Phys. **158**, 194503 (2023).
[39] M. González-Jiménez, T. Barnard, B. A. Russell, N. V. Tukachev, U. Javornik, L.-A. Hayes, A. J. Farrell, S. Guinane, H. M. Senn, A. J. Smith, M. Wilding, G. Mali, M. Nakano, Y. Miyazaki, P. McMillan, G. C. Sosso, and K. Wynne, Understanding the emergence of the boson peak in molecular glasses, Nat. Commun. **14**, 215 (2023).
[40] E. Lerner, G. Düring, and E. Bouchbinder, Statistics and properties of low-frequency vibrational modes in structural glasses, Phys. Rev. Lett. **117**, 035501 (2016).
[41] H. Mizuno, H. Shiba, and A. Ikeda, Continuum limit of the vibrational properties of amorphous solids, Proc. Natl. Acad. Sci. USA **114**, E9767 (2017).
[42] G. Kapteijns, E. Bouchbinder, and E. Lerner, Universal nonphononic density of states in 2D, 3D, and 4D glasses, Phys. Rev. Lett. **121**, 055501 (2018).
[43] L. Wang, A. Ninarello, P. Guan, L. Berthier, G. Szamel, and E. Flenner, Low-frequency vibrational modes of stable glasses, Nat. Commun. **10**, 26 (2019).
[44] D. Richard, K. González-López, G. Kapteijns, R. Pater, T. Vaknin, E. Bouchbinder, and E. Lerner, Universality of the nonphononic vibrational spectrum across different classes of computer glasses, Phys. Rev. Lett. **125**, 085502 (2020).
[45] E. Lerner and E. Bouchbinder, Low-energy quasilocalized excitations in structural glasses, J. Chem. Phys. **155**, 200901 (2021).
[46] C. Rainone, E. Bouchbinder, and E. Lerner, Pinching a glass reveals key properties of its soft spots, Proc. Natl. Acad. Sci. USA **117**, 5228 (2020).
[47] E. Bouchbinder and E. Lerner, Universal disorder-induced broadening of phonon bands: From disordered lattices to glasses, New J. Phys. **20**, 073022 (2018).
[48] Indirect evidence for the $\sim\omega^4$ tail of the nonphononic VDoS has been previously provided through a $\sim T^5$ contribution to the specific heat, e.g., in [20].
[49] C. Rainone, P. Urbani, F. Zamponi, E. Lerner, and E. Bouchbinder, Mean-field model of interacting quasilocalized

excitations in glasses, SciPost Phys. Core **4**, 008 (2021).

[50] E. Bouchbinder, E. Lerner, C. Rainone, P. Urbani, and F. Zamponi, Low-frequency vibrational spectrum of mean-field disordered systems, Phys. Rev. B **103**, 174202 (2021).

[51] R. Kühn and U. Horstmann, Random matrix approach to glassy physics: Low temperatures and beyond, Phys. Rev. Lett. **78**, 4067 (1997).

[52] V. L. Gurevich, D. A. Parshin, and H. R. Schober, Pressure dependence of the boson peak in glasses, Phys. Rev. B **71**, 014209 (2005).

[53] E. Lerner and E. Bouchbinder, Disordered crystals reveal soft quasilocalized glassy excitations, Phys. Rev. Lett. **129**, 095501 (2022).

[54] M. Ramos, J. Moreno, S. Vieira, C. Prieto, and J. Fernandez, Correlation of elastic, acoustic and thermodynamic properties in B_2O_3 glasses, J. Non-Cryst. Solids **221**, 170 (1997).

[55] E. Lerner and E. Bouchbinder, A characteristic energy scale in glasses, J. Chem. Phys. **148**, 214502 (2018).

[56] A. Weiße, G. Wellein, A. Alvermann, and H. Fehske, The kernel polynomial method, Rev. Mod. Phys. **78**, 275 (2006).

[57] Y. M. Beltukov, C. Fusco, D. A. Parshin, and A. Tanguy, Boson peak and Ioffe-Regel criterion in amorphous siliconlike materials: The effect of bond directionality, Phys. Rev. E **93**, 023006 (2016).

[58] C. Rainone, E. Bouchbinder, and E. Lerner, Statistical mechanics of local force dipole responses in computer glasses, J. Chem. Phys. **152**, 194503 (2020).

[59] K. González-López, M. Shivam, Y. Zheng, M. P. Ciamarra, and E. Lerner, Mechanical disorder of sticky-sphere glasses. I. Effect of attractive interactions, Phys. Rev. E **103**, 022605 (2021).

[60] M. Wyart, Correlations between vibrational entropy and dynamics in liquids, Phys. Rev. Lett. **104**, 095901 (2010).

[61] G. Kapteijns, E. Bouchbinder, and E. Lerner, Unified quantifier of mechanical disorder in solids, Phys. Rev. E **104**, 035001 (2021).

[62] K. González-López, E. Bouchbinder, and E. Lerner, Variability of mesoscopic mechanical disorder in disordered solids, J. Non-Cryst. Solids **604**, 122137 (2023).

[63] J. F. Lutsko, Generalized expressions for the calculation of elastic constants by computer simulation, J. Appl. Phys. **65**, 2991 (1989).

[64] C. Maloney and A. Lemaître, Universal breakdown of elasticity at the onset of material failure, Phys. Rev. Lett. **93**, 195501 (2004).